The Cryosphere Discuss., 4, 603–639, 2010
www.the-cryosphere-discuss.net/4/603/2010/

The Cryosphere Discussions

This discussion paper is/has been under review for the journal The Cryosphere (TC).
Please refer to the corresponding final paper in TC if available.

Climate of the Greenland ice sheet using a high-resolution climate model – Part 2: Near-surface climate and energy balance

J. Ettema[1], M. R. van den Broeke[1], E. van Meijgaard[2], and W. J. van de Berg[1]

[1]Institute for Marine and Atmospheric research Utrecht, Utrecht University, Utrecht, The Netherlands
[2]Royal Netherlands Meteorological Institute, De Bilt, The Netherlands

Received: 29 March 2010 – Accepted: 9 April 2010 – Published: 21 April 2010

Correspondence to: J. Ettema (j.ettema@uu.nl)

Published by Copernicus Publications on behalf of the European Geosciences Union.

Abstract

The near-surface climate of the Greenland ice sheet is characterized by persistent katabatic winds and quasi-permanent temperature deficit. Using a high resolution (11 km) regional climate model allows for detailed study of the spatial variability in these phenomena and the underlying atmospheric processes.

The near-surface temperature distribution over the ice sheet is clearly affected by elevation, latitude, large scale advection, meso-scale topographic features and the occurrence of summer melt. The lowest annual temperatures of −30.5 °C are found north of the highest elevations of the GrIS, whereas the lowest southern margins are warmest (−3.5 °C).

Over the ice sheet, a persistent katabatic wind system develops due to radiative surface cooling and the gently slope of the surface. The strongest wind speeds are seen in the northeast where the strong large scale winds, low cloud cover and concave surface force a continuous supply of cold air, which enhances the katabatic forcing. The radiative cooling of the surface is controlled by the net longwave emission and transport of heat towards the surface by turbulence. In summer this mechanism is much weaker, leading to less horizontal variability in near-surface temperatures and wind speed.

1 Introduction

The Greenland ice sheet (GrIS) is the largest permanent ice- and snow covered area in the Northern Hemisphere. The complex orography of the GrIS, with steep gradients along the ice margins, and its high-elevated, smooth interior, is mainly responsible for the variety of regional climates on the ice sheet (Scorer, 1988).

Two meteorological phenomena characterize the near-surface climate of large ice sheets: a quasi-permanent temperature deficit (Van den Broeke et al., 1994) and the persistent low-level katabatic wind circulation (Heinemann, 1999). Due to low absorp-

tion of solar radiation and efficient emission of longwave radiation, the net surface radiation balance becomes negative, resulting in surface cooling and a stable stratification of the atmospheric boundary layer (ABL) (Hoch et al., 2007). This cooling of the near-surface air results in a shallow high air pressure system located over central Greenland, which is the primary driving mechanism for the katabatic winds. These persistent katabatic winds prevent humidity to be transported to the central part of the GrIS at low atmospheric levels (Dethloff et al., 2002).

Many observational studies have been devoted to describe the climate of the GrIS. Steffen and Box (2001) used wind and temperature measurements from 18 GC-Net (Greenland Climate Network) automatic weather stations (AWS) to describe the surface climatology at elevations above 1000 m. Van den Broeke et al. (2008a,b) and Van den Broeke et al. (2008c) focused on the surface energy balance and radiative fluxes in the ablation and percolation zone of west Greenland. Hoch et al. (2007) made year-round radiative flux observations at Summit, the highest point on the GrIS. Earlier meteorological expeditions were mainly restricted to the ablation season rather than year-round observations (Ambach, 1977a,b; Oerlemans and Vugts, 1993; Henneken et al., 1994).

However, large uncertainties remain in observation-based climate studies due to the sparse resolution of measurements in time and/or space. Regional climate models models constitute a powerful mean to fill this space-time gap by determining the climate parameters for the entire ice sheet over longer periods and at high spatial resolution. Due to the high computational costs, most of the previous numerical studies of the GrIS surface climatology cover one ablation season up to 25 years (Cassano et al., 2001; Dethloff et al., 2002; Fettweis, 2007; Hines and Bromwich, 2008).

Here, we present the results of a 51-year integration (1958–2008) with the regional climate model RACMO2/GR. The long term (>30 years) model simulation at high horizontal resolution (11 km) allows a detailed assessment of the regional near-surface climate of the GrIS. In this paper, we present the 51-year means of near-surface parameters wind, temperature, humidity, radiative fluxes, and surface energy balance

(SEB) components of the GrIS.

2 Model description and data analysis

For this study, the Regional Atmospheric Climate MOdel (RACMO2/GR, Van Meijgaard et al., 2008) is used. RACMO2 is based on the HIgh Resolution Limited Area Model (HIRLAM, Undén et al., 2002) and the global model of the European Centrum for Medium-Range Weather Forecasts (ECMWF, updated from cycle 23r4, White, 2004). The model domain of 246×312 grid points covers the entire Greenland ice sheet and part of the surrounding oceans, including Iceland, Svalbard and some Canadian ice caps. The horizontal resolution is 0.10°×0.10°, which corresponds with approximately 11 km; this high resolution is essential in obtaining an accurate representation of the narrow ablation zone, the steep climate gradients on the GrIS and the areas with complicated land-ice sheet-sea contrasts. RACMO2/GR has 40 atmospheric hybrid levels in the vertical. At the lateral boundaries, RACMO2/GR is forced with atmospheric information from ERA-40 (ECMWF Re-Analysis, 1 September 1957–31 August 2002) and ECMWF operation analyses (1 September 2002–1 January 2009). The sea surface temperature and sea ice fraction are prescribed every 6 h.

With respect to the Antarctic version of RACMO2 (Van de Berg et al., 2005), several parameterization schemes have been modified, such as the physical representation of the GrIS snow/firn/ice pack processes (penetration and refreezing of meltwater, heat capacity of the snow/firn pack, surface roughness and albedo) and the air temperature forcing the liquid-solid precipitation ratio. These adaptations have been described in more detail in (Ettema et al., 2010).

Comparison of RACMO2/GR output data with in situ measurements on and around the GrIS showed that the model has some difficulties in simulating the very stable atmospheric conditions, because of a too active mixing scheme that leads to an overestimation of the sensible heat flux SHF. Additionally, the amount of wintertime downwelling longwave radiation is underestimated by ≈25 W m^{-2} that leads to a cold surface bias of

several degrees in places where it is not compensated by the positive SHF bias. These model shortcomings should be kept in mind when reading the remainder of this paper. Otherwise, a good agreement is found with observations, as described in (Ettema et al., 2010).

2.1 Wind

The wind regime on the GrIS is dominated by semi-permanent katabatic winds (Steffen and Box, 2001). Katabatic winds are characterized by a) a maximum in wind speed close to the surface and b) a constant wind direction. An useful tool to detect this persistent circulation is the directional constancy dc defined as the ratio of the vector-averaged wind speed to the mean wind speed usually taken at 10 m (Bromwich, 1989):

$$dc = \frac{\left(\overline{u}^2 + \overline{v}^2\right)^{\frac{1}{2}}}{\left(u^2 + v^2\right)^{\frac{1}{2}}} \quad (1)$$

where u and v are the horizontal components of the 10 m wind. A dc of zero implies that the near-surface wind direction is random; when dc is 1, the wind blows continuously from one direction.

2.2 Temperature

The near-surface air temperature $T_{2\,\mathrm{m}}$ depends strongly on elevation and maximum solar zenith angle. To remove most of the elevation dependency, we compute the potential temperature θ defined as the temperature an air parcel would have if it were brought to sea level without heat exchange with its surroundings:

$$\theta_v = T_v \left(\frac{p_0}{p}\right)^{\frac{R_d}{c_p}} = (T + 0.61q) \left(\frac{p_0}{p}\right)^{\frac{R_d}{c_p}} \quad (2)$$

where T is the air temperature, T_v the virtual air temperature, p the air pressure, p_0=1000 hPa the reference pressure, R_d=287 J kg^{-1} K^{-1} the gas constant of the dry atmosphere, and c_p=1005 J kg^{-1} K^{-1} the specific heat of air at constant pressure and q the specific humidity introduced to take the effect of moisture on the buoyancy of the air parcel into account.

As the GrIS spans roughly 2600 km from the northernmost point at Cape Morris Jesup to the southern tip at Cape Farwell, the northern part of the ice sheet receives on an annual basis a considerably smaller amount of solar radiation than the southern regions. Reeh (1991) presented a linear regression of the ice sheet mean annual near-surface air temperature $T_{2\ \mathrm{m,Reeh}}$ expressed as a function of elevation E and latitude L based on a study by Ohmura (1987):

$$T_{2\ \mathrm{m,Reeh}} = 48.83 - 0.007924E - 0.7512L \quad (3)$$

Another key factor affecting the near-surface air temperature is the radiative cooling of the surface, mainly in winter, leading to a quasi-permanent temperature inversion. A common measure for the strength of this inversion is the temperature perturbation Δ_θ, which is the difference between the ABL potential temperature and the potential temperature observed in the free troposphere extrapolated to the same height (Van den Broeke and van Lipzig, 2003). A large negative value of Δ_θ indicates a strong temperature inversion in the ABL. To calculate Δ_θ, we assume a linear background potential temperature profile that fits best to the free atmosphere potential temperatures. This means that the lapse rate $\gamma_\theta = \partial\theta/\partial z$ of the background potential temperature $\theta_0(z)$ is assumed constant with height z in the free atmosphere:

$$\theta_0(z) = \theta_0(0) + \gamma_\theta z \quad (4)$$

$\Delta_\theta(z)$ is then defined as the potential temperature perturbation relative to the undisturbed background or free atmosphere by:

$$\Delta_\theta(z) = \theta(z) - \theta_0(z) \quad (5)$$

Vertical integration of Δ_θ over the ABL provides insight in the spatial distribution of cold air accumulation:

$$\hat{\theta} = \int_0^h \Delta_\theta(z)dz \tag{6}$$

where the height h is chosen well above the top of the temperature deficit layer (TDL) to avoid having to define the height of the stable ABL, which is poorly constrained under stable conditions.

2.3 Surface energy balance

The air temperature near the surface is strongly coupled to the surface temperature T_s. When radiation penetration into the snowpack is neglected T_s is fully determined by the surface energy balance (SEB), which is defined as

$$\begin{aligned} M &= \mathrm{SW}_\downarrow(1-\alpha) + \epsilon\mathrm{LW}_\downarrow - \epsilon\sigma T_s^4 + \mathrm{SHF} + \mathrm{LHF} + G_s \\ &= \mathrm{SW}_{\mathrm{net}} + \mathrm{LW}_{\mathrm{net}} + \mathrm{SHF} + \mathrm{LHF} + G_s \end{aligned} \tag{7}$$

where M is the melt energy, $\mathrm{SW}_\downarrow$, $\mathrm{SW}_\uparrow$, $\mathrm{LW}_\downarrow$, $\mathrm{LW}_\uparrow$ are the downward and upward directed fluxes of solar and infrared radiation, α is the broadband surface albedo, ϵ the surface emissivity for longwave radiation ($\epsilon = 0.98$ is used in RACMO2/GR for the ice sheet), σ the Stefan-Boltzmann constant, LHF and SHF the turbulent fluxes for latent and sensible heat, and G_s the subsurface conductive heat flux at the surface. All terms are defined as positive when directed towards the surface.

SHF and LHF depend on the temperature, wind and humidity fluctuations in the surface layer (SL):

$$\begin{aligned} \mathrm{SHF} &= -\rho c_p \overline{(w'\theta')} = \rho c_p u_* \theta_* \\ \mathrm{LHF} &= -\rho L_s \overline{(w'q')} = \rho L_s u_* q_* \\ u_* &= \sqrt{\tau/\rho} \end{aligned} \tag{8}$$

where ρ is the air density, c_p the heat capacity of dry air at constant pressure, L_s the latent heat of sublimation, w', θ' and q' are the turbulent fluctuations of vertical velocity, potential temperature and specific humidity, u_*, θ_* and q_* the associated turbulent scaling parameters, and τ the wind shear or horizontal momentum flux.

In RACMO2/GR, the SEB is iteratively solved for the surface temperature using Monin-Obukhov similarity theory for the turbulent fluxes with the stability functions of Holtslag and Bruin (1988) for stable and Dyer (1974) for unstable conditions. Since u_*, θ_* and q_* are not available in the model output, their values have been derived from mean annuals for the turbulent heat fluxes, to provide insight in the relative contribution of wind shear, specific humidity and temperature gradients to the turbulent heat fluxes.

3 Surface climate

In this section, we present mean annual (1 January–31 December) values of the surface climate variables air pressure, temperature, wind and SEB components as simulated by RACMO2/GR averaged over the period 1958–2008.

3.1 Large scale circulation

Figure 1 shows the 1958–2008 annual, winter (DJF) and summer (JJA) sea level pressure (dashed lines) and height of the 500 hPa level Z_{500} (solid lines). The mean surface level pressure is not plotted over land, because the topography of the GrIS and the strong density profiles make downward interpolation highly uncertain. The 500 hPa level is chosen here, because it is the first standard pressure level that does not intersect with the ice sheet surface and lies well above the surface layer (SL).

The GrIS is situated just poleward of the polar front; the strong baroclinicity results in a westerly upper air flow and an easterly near-surface flow. Because it is also situated in the northward directed branch of the standing planetary waves in the Northern Hemisphere (NH), the 500 hPa circulation is directed southwest-northeast, forcing upper-air

southwesterlies over the GrIS that constitute the so-called polar vortex. RACMO2/GR is well capable of realistically simulating these large scale circulation patterns (Fig. 1), as expected because of the use of lateral forcing from ECMWF analyses.

The North Atlantic main storm tracks are located around Greenland and cause relatively high accumulation rates over western and southeastern Greenland (Ohmura and Reeh, 1991; Steffen and Box, 2001; Ettema et al., 2009). The net effect of the individual low pressure systems results in a climatologic low pressure system (1004.5 hPa) located over the Irminger Sea, the so-called Icelandic Low. The wintertime Icelandic Low is relatively deep (below 1000 hPa) and positioned close to the east coast of south Greenland, while in summer the low is more shallow (about 1009 hPa) and centered close to the south coast of Iceland. The center and depth of the Icelandic Low is well represented in RACMO2/GR.

With elevations over 3000 m, the GrIS acts as a barrier for weather systems in the North Atlantic region. It prevents cyclones to move directly from west to east across the ice sheet. Rather, the main pathways are northward along the western flank or eastward south of the GrIS, and retrogade eastwards at higher latitudes (Scorer, 1988). Locally, the steep topographic gradients in southeast Greenland have a pronounced effect on the synoptic systems, e.g. by splitting low air pressure systems at the southern tip of Greenland, by distortion of the wind and temperature fields and by inducing cyclogenesis in the lee-side of the steep slopes in the south (Tsukernik et al., 2007).

3.2 Near-surface wind

Over the GrIS, the annual mean 10 m wind speeds (1958–2008 average) range from 1.5 to 10.3 m s^{-1} (Fig. 2a). The lowest mean annual wind speeds are found over the tundra and adjacent ice sheet along the northern and western margins. The decreasing wind speed at 10–20 km from the ice edge is confirmed by AWS observations (Duynkerke and van den Broeke, 1994; Van den Broeke et al., 2008c). This deceleration of the katabatic flow is partly caused by increasing surface roughness lengths due to a rougher ice surface in the ablation zone, and also by the diurnal variation in the

thermally forced wind imposed by the flat tundra close to the ice edge. This thermal wind forcing is associated with cold air pooling over the tundra (Van den Broeke et al., 1994, 2002; Gallée and Pettré, 1998).

The largest simulated wind speeds on the ice sheet occur in northeast Greenland over Dronning Louise Land and to its south. Unfortunately, no direct meteorological observations are available for this region. The AWS locations NASA-E and Tunu-N from GC-Net are located higher up the ice sheet (Steffen and Box, 2001). Wind speeds in winter (DJF, Fig. 2b) are generally larger than in summer (JJA, Fig. 2c). In winter, cloud cover is low and there is enhanced radiative surface cooling, as discussed in Sect. 3.5, leading to stronger katabatic forcing. Furthermore, the polar vortex is stronger in winter, as it is proportional to the large-scale temperature gradient between the North Pole and the equator, which is largest in wintertime; as in Antarctica, the large scale pressure gradient force (PGF) acts to support the katabatic PGF over the ice sheet (Van den Broeke et al., 2002).

The mean wind vector shows a clear outflow of air over the ice sheet surface. The mean wind direction is downslope with a deflection to the right due to the Coriolis force. Assuming a continuous katabatic forcing and steady state without friction, the flow would be along the elevation contours. Friction normally maintains a downslope component, but apparently, the west coast of Greenland is strongly influenced by the low-pressure systems in the northern Baffin Bay, resulting in a flow almost parallel to the elevation contours. This corresponds well with observations of Steffen and Box (2001).

The katabatic winds over the ice sheet are persistent throughout the year, which is reflected in a high mean value of dc ($\approx$0.6) for the majority of the GrIS (Fig. 3a). The largest values of dc (>0.9) coincide with areas of strong katabatic winds. The katabatic wind system dissipates after crossing the ice edge, resulting in low wind speeds and low values for dc over the tundra. On the ice sheet, the lowest values for dc are found on the two domes and the ridge in between. Here, the wind direction is governed by the large scale circulation, since the katabatic wind system is weakly developed in these

areas in the absence of a significant surface slope.

The 10 m wind direction over the adjacent oceans is highly variable. Throughout the year, a clear wind maximum (>14 m s^{-1}) is located south of the southern most tip of Greenland with a rather low value for dc of 0.3. Here, the steep and high topography of the GrIS results in significant atmospheric flow distortion that leads to a common occurrence of high surface wind speeds in its surrounding area, the so-called the Greenland tip jet (Moore and Renfrew, 2005). The low dc can be explained by the bimodality of the zonal wind in this area with high wind speed events occurring from both directions.

The regional high wind speeds along the southeastern coast at ~66° N are more persistent throughout the year. Figure 2b shows that the cold and stable stratified katabatic outflow through the numerous fjords is forced back towards the topographic barrier by the prevailing synoptic-scale easterly flow. This so-called barrier wind is seen in more detail when zooming in on this region and plotting the DJF averaged wind vectors at the full model resolution of 11 km (Fig. 3b). Moore and Renfrew (2005) observed these barrier winds in the near-surface wind speed fields derived from QuickScat data. It confirms the ability of RACMO2/GR to simulate the regional wind climate accurately, not only on the ice sheet, but also over the surrounding oceans, which is benificial for forcing of regional ocean models.

3.3 Near-surface temperature

Figure 4 shows the mean annual, winter and summer 2 m temperature and sea ice extent (shaded) where the ocean is ice-covered for more than 75% of the time (average 1958–2008). The sea ice cover generally is most extensive in spring and could lead to a time lag in temperature minimum on some coasts (Scorer, 1988). The annual air temperature over the GrIS ranges from −30.5 to −3.5 °C. The lowest temperatures are found north of the highest elevations of the GrIS, which is in agreement with the findings of Chen et al. (1997) and Cassano et al. (2001). The climate at the eastern side of Greenland is colder compared to the western side at the same altitude. This agrees with the findings of Steffen and Box (2001). A possible cause for this could be

the insulating effect of the sea ice present along the north and northeastern coastline of Greenland and the advection of cold air by downslope winds.

During wintertime, the absence of sunlight and the presence of sea ice result in very low air temperatures in the northern regions (Fig. 4b). In summer, the melting snow/ice at the surface limits the air temperature to close to the melting point along the ice margins (Fig. 4c). The highly elevated interior shows the largest variability in daily mean $T_{2\,\mathrm{m}}$. Here, the daily winter temperature can drop below −70 °C, while in summer the temperature can rise close to the melting point. The lowest variability is found along the lower margins in the southeast, where the temperature is governed by advection of warm and humid (cloudy) air throughout the year. Because everywhere on the GrIS, the mean temperature for the warmest month is below 10 °C, the climate of the GrIS can be classified as Arctic. Only where the land strip is wider than 100 km and becomes snow free in summer does the July temperature rise above this threshold. These northeastern and western tundras have a subarctic climate.

The near-surface temperature is evidently affected by surface elevation, latitude and the sea ice extent. Figure 5a shows that the influence of the surface elevation can be largely removed by considering the 2 m potential temperature $\theta_{2\,\mathrm{m}}$ (Eq. 2). The south dome at the GrIS experiences the highest $\theta_{2\,\mathrm{m}}$, which generally decreases with latitude. The high $\theta_{2\,\mathrm{m}}$ values over the southern and southeastern GrIS signify frequent advection of warm maritime air. The low values over the northern tundra are caused by the absence of katabatic wind and warm air advection, enabling a strong inversion to build up. Over the adjacent oceans, $\theta_{2\,\mathrm{m}}$ is clearly affected by the presence of sea ice, insulating the warm ocean from the atmosphere.

Figure 5b shows the difference between annual mean $T_{2\,\mathrm{m,Reeh}}$ as computed with Eq. (3) and $T_{2\,\mathrm{m}}$ simulated by RACMO2/GR. This comparison confirms that elevation and latitude are of major influence on the near-surface temperature, but can not entirely explain the temperature distribution in Fig. 4a. The difference ranges from −5 °C in the eastern regions to +6 °C close to the northern ice margins. The empirical function generally underestimates $T_{2\,\mathrm{m}}$ by 1 to 3 °C. Positive biases occur only along the lowest

ice sheet margins (<750 m). The GrIS averaged bias of −1.4 °C implies that other processes affect the near-surface temperature as well. Neglecting the recent warming since the 1990s (Hanna et al., 2008) and considering the model output for the period 1958–1990 only, the bias decreases to −1.2 °C averaged over the ice sheet. All in all, the agreement is quite good, given the simplicity of the empirical relation.

3.3.1 Potential temperature deficit Δ_θ

Figure 6a shows the annual background surface potential temperature $\theta_0(0)$ (Eq. 4). $\theta_0(0)$ is generally higher than the actual surface potential temperature, $\theta(0)$, implying that the free atmosphere is potentially warmer than the ABL. A clear northwest-southeast gradient is seen over the ocean, which corresponds with the spatial variability in the geopotential height at the 500-hPa level (Fig. 1). The highest values of $\theta_0(0)$ are found over the higher elevations of the GrIS, indicative of the stable stratification of the free atmosphere (γ_θ>0, Fig. 6d). The free atmosphere is less stably stratified over the convective area in the surroundings of the Icelandic Low.

The annual potential temperature perturbation at the surface $\Delta_\theta(0)$ is depicted in Fig. 6b. A strong temperature deficit (>10 °C) is restricted to the northeastern part of the ice sheet and the sea ice covered areas with smaller values on the southern and western lower ice margins, and over open ocean water. Over the GrIS, a dependency of the temperature deficit on the topography, cloud cover (see later) and the presence of nearby sea ice is visible. Strongest temperature perturbations (more than 13 °C) are found on the northeastern slopes, where also the strongest katabatic winds occur. We speculate that southeasterly large scale winds (Fig. 1) force a continuous supply of cold air from the higher elevated parts of the ice sheet to this area. Moreover, the ice sheet surface topography forces a regional convergence of the winds in this area, prohibiting the ABL to heat up by divergence and associated subsidence. The result is that the air remains cold and katabatic winds strong. In comparison to the Antarctic plateau (Van de Berg et al., 2008) we find considerably smaller values for the temperature deficit on the GrIS, because Greenland experiences a regular large scale advection of warm air

from the sea ice-free Atlantic Ocean and is in general situated in a more temperate climate zone.

Figure 6c shows the vertically integrated temperature perturbation $\hat{\theta}$ (Eq. 6). The greatest magnitudes are found just seaward of the northeast Greenland coastline, where the ocean is covered by sea ice for 50 to 95% of the year. This flat area acts as a collector of cold air that drains from the GrIS. The values over the ice sheet become more negative towards the margins, suggesting that katabatic outflow of cold air over the surface is compensated by a continuous subsidence of warmer air from the free atmosphere, diminishing the vertical extent of the TDL and hence $\hat{\theta}$.

3.4 Near-surface humidity

Figure 7 depicts that the annual mean 2 m relative humidity $RH_{2\,m}$ (average 1958–2008) decreases towards the ice margins, while the 2 m specific humidity $q_{2\,m}$ increases. $RH_{2\,m}$ is lowest in glacial valleys in the northeast. The strong katabatic winds advect cold, dry air from the ice sheet interior and meanwhile the katabatic system prevents humidity transport towards the northeast. In summer, the air warms the tundra and consequently $RH_{2\,m}$ is reduced. In contrast, $q_{2\,m}$ increases, because the higher temperatures allow an exponentially higher maximum moisture content, dominating the decrease in $RH_{2\,m}$. Due to the strong correlation between temperature and specific humidity, the spatial pattern of $q_{2\,m}$ is very similar to the distribution of $T_{2\,m}$ (Fig. 4a), with the lowest values in the cold interior and the warmer air containing more moisture along the southern ice margins.

3.5 Surface energy balance

The surface energy balance (SEB) determines the surface temperature and melt whenever T_s=273.16 K (Eq. 7). The radiative fluxes contribute importantly to the ice sheet SEB, whereas the turbulent heat fluxes are expected to be smaller than in midlatitude climates. The subsurface heat flux G_s is expected to play a minor role in the annual

mean SEB. If the sum of all these SEB components is positive, the remaining energy is used for melting the snow/firn/ice pack, M. Observations show that net radiation provides a significant part of the energy used for melt in the ablation zone, in spite of the relatively high surface albedo (e.g. Duynkerke and van den Broeke, 1994; Konzelmann and Braithwaite, 1995 and Van den Broeke et al., 2008b).

3.5.1 Net surface solar radiation and surface albedo

The snow/firn surface of the GrIS has a high albedo α and hence reflects the incoming solar radiation $SW_{\downarrow}$ effectively. Over central Greenland, the mean α is about 0.825, which corresponds with the albedo of fresh snow (Fig. 8a). Consequently, the largest part of $SW_{\downarrow}$ is reflected and the fraction absorbed at the surface SW_{net} reaches values between 20 and 25 W m^{-2} (Fig. 8b). These values correspond well with the observed mean values for albedo (0.82) and net solar radiation (24 W m^{-2}) at Summit averaged over the period July 2000–July 2002 (Hoch, 2005).

The albedo decreases towards the ice margins due to growing snow grains in the snow/firn/ice pack during spring and summer melt periods. In the percolation zone, the decrease in α (α~0.7) is associated with moistening of the snow pack, while in the ablation zone, in addition, the relatively dark glacier ice (α~0.5) is at the surface during a few days up to weeks or even months per year. That is why SW_{net} increases to almost 50 W m^{-2} along the ice margins, implying more shortwave radiation energy available for melt. On the adjacent tundra, the values for SW_{net} are even higher (~70 W m^{-2}) due to the low summer albedo (α~0.18) of the snow free tundra surface.

3.5.2 Cloud cover and longwave radiation

Information about clouds is valuable for a correct interpretation of temporal and spatial variability of radiative fluxes. Figure 9a shows that the total cloud cover decreases sharply from the interior ice sheet (>0.9) towards the ice margin, with the lowest values of 0.45 found in the northeast. The high amount of cloud cover in the interior frequently

only consists of a shallow near-surface fog layer, confirmed by observations at Summit during summer nights (Hoch et al., 2007). However, the effect of clouds on radiation is primarily determined by the presence of liquid water and ice in the atmosphere. Total cloud cover does not provide quantitative information on radiative scattering properties of the atmosphere, because it is no good measure for the optical thickness of the cloud. Therefore, we analyzed the atmospheric SW transmissivity, defined as the ratio between the incoming SW at the surface and at the top of the atmosphere, which depends on the amount and vertical distribution of water vapor, clouds, atmospheric mass and aerosols. Figure 9b shows that SWtransmissivity reveals a different spatial pattern. It increases with elevation, caused by a shorter associated atmospheric pathway for solar radiation. The low cloud cover in northeast Greenland coincides with relatively high values in SWtransmissivity, indicative for dry air advected by the strong katabatic winds. Note that Summit, besides having the highest mean cloud cover, still has very high transmissivity. This indicates that the simulated cloud layer must be very thin or only occurs at low sun angles, which is typical for radiative fog.

Incoming infrared radiation $LW_{\downarrow}$ is a function of the temperature and humidity distribution in the lowest atmospheric layers, but also of low level clouds, which determine the atmospheric radiative longwave properties. Therefore, $LW_{\downarrow}$ (not shown) shows large similarities (albeit reversed) with the SW transmissivity. The outgoing LW radiation $LW_{\uparrow}$ is determined by the surface temperature, leading to simulated net emitted longwave radiation LW_{net} between −30 and −60 W m^{-2} (Fig. 10a). RACMO2/GR is known to underestimate $LW_{\downarrow}$ during winter months (Ettema et al., 2010; Van de Berg et al., 2008). Therefore, the modeled LW_{net} values are likely too low.

The negative LW_{net}, and the associated cooling of the surface, indirectly forces the katabatic circulation over Greenland, which prevents or reduces cloud cover and contributes to the development of the Greenland shallow high pressure system. In general, the heat loss due to LW emission increases towards lower elevations, with maximum values in Dronning Louise Land (Fig. 10a). Characteristic for this area are the very strong katabatic winds that bring cold, dry air from the interior, and the absence of

large scale advection of moist air, both reducing the moisture content of the overlying air and thus $LW_{\downarrow}$. Moreover, the katabatic winds effectively heat the surface through SHF, increasing T_s and $LW_{\uparrow}$ and enhancing the radiative heat loss.

In the western lower ablation zone, LW_{net} decreases again with altitude. Here, the emission of LW radiation is limited in summer due to continuous melting at the surface, which causes a smaller LW radiative heat loss than for areas where the melting is intermittent during the melt season (Van den Broeke et al., 2008a).

3.5.3 Net radiation

The sum of SW_{net} and LW_{net} equals the net radiation (Fig. 10b). Net radiation is on average negative everywhere on the ice sheet, implying that the heat loss by LW_{net} is larger than the absorption of solar radiation. This heat loss decreases sharply to zero close to the ice sheet margin, where the relatively smaller heat loss due to LW is compensated by the increased SW absorption due to the low albedo. Observations by Van den Broeke et al. (2008a) confirm that small positive annual values can occur at 6 km from the ice margin, while small negative values are observed in the higher ablation and percolation zone, in very good agreement with Fig. 10b. The net radiative cooling has to be compensated by the subsurface heat flux and, in particular, turbulent heat fluxes.

3.5.4 Turbulent fluxes of sensible and latent heat

The turbulent scales of momentum u_*, moisture q_* and heat θ_* are computed to provide insight in the relative contributions of the wind, humidity and temperature near-surface gradients to the surface latent and sensible heat fluxes, SHF and LHF (Eq. 8). The spatial distribution of θ_* (Fig. 11a) shows similarities (albeit reversed) with potential temperature (Fig. 5a) and surface temperature deficit (Fig. 6b). Positive/negative θ_* means that the SL is on average stably/unstably stratified. The radiative cooling of the surface enforces positive θ_* values and a stable ABL over the ice sheet interior.

Negative θ_* are found over the ocean, where convection occurs when cold air is transported over the warm ocean water. The warm sea water of the North Atlantic Drift to the south of Greenland allows the surface temperature to rise above the temperature of the overlying atmosphere.

Figure 11b shows that annual mean q_* decreases and becomes negative towards the ice sheet margins, signifying sublimation/evaporation. In the dry snow zone, q_* remains positive throughout the year, an indication for net deposition. Below 2000 m elevation, the surface-to-air specific humidity gradient is very small in winter in response to the low temperatures. In spring and summer, the surface is heated, but not yet melting, leading to strongly negative values for q_* implying sublimation. Here, the magnitude of q_* is much larger in summer than in winter resulting in negative values on an annual basis.

The spatial distribution of u_* (Fig. 11c) qualitatively follows the 10 m wind speed (Fig. 2a). The increasing surface roughness towards the margins enhances u_*. These high values along the margins are necessary to maintain mechanical generation of turbulence in the stably stratified ABL (Van den Broeke et al., 2008c).

In the ice sheet interior, the relatively large values of θ_* coincide with low friction velocities, leading to a rather homogeneous distribution of SHF ($\sim u_*\theta_*$) as seen in Fig. 12a. The positive SHF values indicate cooling of the ABL and heating of the surface. The annual SHF increases towards the margins to maximum values of +38 W m^{-2} at about 50 km from the ice edge, except for the southeastern part of the ice sheet. This enhancement can be ascribed mostly to the positive coupling between u_* and θ_*. Strong radiative cooling leads to large θ_*, which through katabatic forcing enhances u_*, leading to large values of SHF as long as the radiative cooling is maintained. The decreasing SHF at the ice edge is the result of the deceleration of the katabatic winds, as found in the northern and western parts of Greenland. Over the ice sheet, SHF almost fully compensates the radiative heat loss. Over the surrounding oceans, negative values for SHF are found, because on average cold air flows over a relatively warm sea surface. An exception is the area with seasonal sea ice cover, which insulates the

warm ocean from the atmosphere and experiences net warming by SHF.

Over the ice sheet, the magnitude of LHF ($\sim u_* q_*$) is much smaller than SHF (Fig. 12b). Deposition (LHF>0) dominates in the interior of the GrIS, while sublimation (LHF<0) prevails in the ablation and percolation zone. This pattern can be ascribed to q_*. Deposition occurs at elevations over 2000 m throughout the year and is associated with the strong surface temperature inversions due to radiative cooling. Relatively strong sublimation occurs at lower altitudes, especially in spring when the snow is not melting.

The modeled LHF agrees well with the sublimation map based on GC-net observations along or above the equilibrium line altitude (Box and Steffen, 2001), except for the southwestern lower ablation zone where the modelled LHF decreases close to the ice edge. Here, sublimation changes regularly into deposition in summer as a result of fixed T_s during melt. These summer reversals occur less frequently with increasing elevation, and here sublimation dominates in summer. This model result agrees with AWS observations made in the southwestern ablation zone by Van den Broeke et al. (2008c). The summertime sublimation ($\sim -10\,\mathrm{W\,m^{-2}}$ for July) in the percolation zone absorbs part of the energy that would otherwise be available for melting. This implies that despite its relatively small magnitude LHF plays an important role in maintaining the ice sheet, as was already suggested by Henneken et al. (1994).

3.5.5 Melt energy and subsurface heat flux

Figure 13 shows the 1958–2008 maps for the annual mean subsurface heat flux, G_s and melt energy, M. They depict similar patterns over the ice sheet, nevertheless the energy available for melt is a magnitude larger than it is for G_s. The heat gain from the lower snow/firn/ice layers towards the surface increases from near zero in the dry snow zone to $+4.5\mathrm{W\,m^{-2}}$ at the margins. In the percolation zone, G_s is mostly positive during summer, because of the heat release in the snow pack due to refreezing of melt water. Closer to the ice edge in western Greenland, the mean G_s is found to slightly decrease. In these areas, G_s is small in summer, because the upper ice layers become isothermal

due to the continuous melting. This feature is confirmed by measurements along the K-transect by Van den Broeke et al. (2008b). In winter, the surface is everywhere colder than the underlying snow, resulting in a negative G_s (not shown). Only in areas without significant M, does the annual average of G_s become zero.

There is an obvious correlation between the amount of melt M and the values of surface albedo α (Fig. 8a). Low values of α coincide with a large M, because a darker surface absorbs more solar radiation, which becomes available for melting once the surface temperature is at the melting point. In turn, this melting lowers α further until the bare glacier ice is at the surface, inducing the onset of a positive feedback mechanism that lasts until the first snowfall event increases the albedo. Konzelmann and Braithwaite (1995) found the same correlation based on observations of the daily ablation and the estimated albedo at ETH Camp in the western ablation zone.

4 Summary and conclusions

A 51-year simulation (1958–2008) of the climate of the GrIS and its immediate surroundings has been performed with the regional atmospheric climate model RACMO2/GR at 11-km resolution, driven by ERA-40 and ECMWF operational analyses at the lateral boundaries and sea surface. A detailed analysis of the model simulated near-surface climate (temperature, wind, humidity, atmospheric and surface properties, and SEB) averaged over this period is presented in this paper.

Key factors determining the near-surface temperature are elevation, latitude, cloud cover, large scale heat advection, and the occurrence of melt. As a result, the lowest annual temperatures are found at the higher elevations north of Summit. The ice sheet surface temperature deficit is caused by a negative net radiation, which is mainly balanced by a downward sensible heat flux. As a result, the ABL cools and cold air flows away from the interior of the ice sheet as persistent katabatic flows that are directed towards the ice sheet margins. On the GrIS, the largest wind speeds are found in the northeast, where radiative cooling is largest due to low cloud cover. Moreover, the con-

cave surface and a synoptic pressure gradient favorable for advection of cold air keep the air cold, further enhancing the katabatic forcing. Near the top of the ice sheet in absence of katabatic forcing, the large scale pressure gradient force is the dominant factor controlling the near-surface wind field.

In the ablation zone, the net radiation increases due to enhanced solar radiation absorption by the darker surface. Due to strong vertical mixing by the katabatic winds, the SHF is large enough to compensate most of the radiative heat loss. Sublimation is enhanced at the margins as a result of the higher temperatures. As soon as the snow/firn/ice surface reaches the melting point, the remaining energy at the surface is available for melt.

In summary, the GrIS has a large spatial variability in near-surface climate parameters.

References

Ambach, W.: Untersuchungen zum Energieumsatz in der Ablationszone des Grönländischen Inlandeises, Expedition Glaciologique Internationale au Groenland, 4, 63, Bianco Lunos Bogtrykkeri A/S, Kopenhagen, 1977a. 605

Ambach, W.: Untersuchungen zum Energieumsatz in der Akkumulationszone des Grönländischen Inlandeises, Expedition Glaciologique Internationale au Groenland, 4, 44, Bianco Lunos Bogtrykkeri A/S, Kopenhagen, 1977b. 605

Box, J. E. and Steffen, K.: Sublimation on the Greenland ice sheet from automated weather station observations, J. Geophys. Res., 106, 33965–33981, 2001. 621

Bromwich, D. H.: An extraordinary katabatic wind regime at Terra Nova Bay, Antarctica, Mon. Weather Rev., 117, 688–695, 1989. 607

Cassano, J. J., Box, J. E., Bromwich, D. H., Li, L., and Steffen, K.: Evaluation of Polar MM5 simulations of Greenland's atmospheric circulation, J. Geophys. Res., 106, 33867–33889, 2001. 605, 613

Chen, Q.-S., Bromwich, D. H., and Bai, L.: Precipitation over Greenland retrieved by a dynamic method and its relation to cyclonic activity, J. Climate, 10, 839–870, 1997. 613

Dethloff, K., Schware, M., Christensen, J. H., Kiilsholm, S., Rinke, A., Fischer, H., Kipfstuhl,

S., and Miller, H.: Recent Greenland accumulation estimated from regional climate model simulations and ice core analysis, J. Climate, 15, 2821–2832, 2002. 605
Duynkerke, P. G. and van den Broeke, M. R.: Surface energy balance and katabatic flow over glacier and tundra GIMEX-91, Global Planet. Change, 9, 17–28, 1994. 611, 617
Dyer, A. J.: A review of flux-profile relationships, Bound.-Lay. Meteorol., 7, 363–372, 1974. 610
Ettema, J., van den Broeke, M. R., van Meijgaard, E., van de Berg, W. J., Bamber, J. L., Box, J. E., and Bales, R. C.: Higher surface mass balance of the Greenland ice sheet revealed by high-resolution climate modeling, Geophys. Res. Lett., 36, L12501, doi:10.1029/2009GL038110, 2009. 611
Ettema, J., van den Broeke, M. R., van Meijgaard, E., van de Berg, W. J., Box, J. E., and Steffen, K.: Climate of the Greenland ice sheet using a high-resolution climate model – Part 1: Evaluation, The Cryosphere Discuss., 4, 561–602, 2010, http://www.the-cryosphere.net/4/561/2010/. 606, 607, 618
Fettweis, X.: Reconstruction of the 1979–2006 Greenland ice sheet surface mass balance using the regional climate model MAR, The Cryosphere, 1, 21–40, 2007, http://www.the-cryosphere-discuss.net/1/21/2007/. 605
Gallée, H. and Pettré, P.: Dynamical constraints on katabatic wind cessation in Adélie Land, Antarctica, J. Atmos. Sci., 55, 1755–1770, 1998. 612
Hanna, E., Huybrechts, P., Steffen, K., Cappelen, J., Huff, R., Shuman, C., Irvine-Fynn, T., Wise, S., and Griffiths, M.: Increased runoff from melting from the Greenland ice sheet: a response to global warming, J. Climate, 21, 331–341, doi:10.1175/2007JCLI1964.1, 2008. 615
Heinemann, G.: The KABEG'97 field experiment: an aircraft-based study of katabatic wind dynamics over the Greenland ice sheet, Bound.-Lay. Meteorol., 93, 75–116, doi:10.1023/A:1002009530877, 1999. 604
Henneken, E. A. C., Bink, N. J., Vugts, H. F., Cannemeijer, F., and Meesters, A. G. C. A.: A case study of the daily energy balance near the equilibrium line on the Greenland ice sheet, Global Planet. Change, 9, 69–78, 1994. 605, 621
Hines, K. M. and Bromwich, D. H.: Development and testing of polar weather research and forecasting (WRF) model. Part I: Greenland ice sheet meteorology, Mon. Weather Rev., 136, 1971–1989, doi:10.1175/2007MWR21112.1, 2008. 605
Hoch, S.: Radiative flux divergence in the surface boundary layer, a study based on observations at Summit. Greenland, Ph.D. thesis, Swiss Federal Institute of Technology (ETH)

Zurich, 2005. 617
Hoch, S. W., Calanca, P., Philipona, R., and Ohmura, A.: Year-round observation of long-wave radiative flux divergence in Greenland, J. Appl. Meteorol., 46, 1469–1479, doi: 10.1175/JAM2542.1, 2007. 605, 618
Holtslag, A. A. M. and Bruin, H. A. R. D.: Applied modelling of the night-time surface energy balance over land, J. Appl. Meteorol., 27, 689–704, 1988. 610
Konzelmann, T. and Braithwaite, R. J.: Variation of ablation, albedo and energy balance at the margin of the Greenland ice sheet, Kronprins Christian Land, eastern north Greenland, J. Glaciol., 41, 174–182, 1995. 617, 622
Moore, G. W. K. and Renfrew, I. A.: Tip jet and barrier winds: a Quickscat climatology of high wind speed events around Greenland, J. Climate, 18, 3713–3725, 2005. 613
Oerlemans, J. and Vugts, H. F.: A Meteorological experiment in the melting zone of the Greenland ice sheet, B. Am. Meteorol. Soc., 74, 3–26, 1993. 605
Ohmura, A.: New temperature distribution maps for Greenland, Z. Gletscherkd. Glazialgeol., 23, 1–45, 1987. 608
Ohmura, A. and Reeh, N.: New precipitation and accumulation maps for Greenland, J. Glaciol., 37, 140–148, 1991. 611
Reeh, N.: Parameterization of melt rate and surface temperature on the Greenland ice sheet, Polarforschung, 59(3), 113–128, 1991. 608
Scorer, R. S.: Sunny Greenland, Q. J. Roy. Meteorol. Soc., 114, 3–29, 1988. 604, 611, 613
Steffen, K. and Box, J. E.: Surface climatology of the Greenland Ice sheet: Greenland Climate Network 1995–1999, J. Geophys. Res., 106, 33951–33964, 2001. 605, 607, 611, 612, 613
Tsukernik, M., Kindig, D. N., and Serreze, M. C.: Characteristics of winter cyclone activiy in the northern North Atlantic: insights from observations and regional modelling, J. Geophys. Res., 112, D03101, 2007. 611
Undén, P., Rontu, L., Järvinen, H., Lynch, P., Calvo, J., Cats, G., Cuxart, J., Eerola, K., Fortelius, C., Garcia-Moya, J. A., Jones, C., Lenderink, G., McDonald, A., McGrath, R., Navascues, B., WoetmanNielsen, N., Ødegaard, V., Rodriguez, E., Rummukainen, M., Rõõm, R., Sattler, K., Sass, B. H., Savijärvi, H., Schreur, B. W., Sigg, R., The, H., and Tijm, A.: High Resolution Limited Area Model, HIRLAM-5 scientific documentation, Tech. rep., Swed. Meteorol. and Hydrol. Inst, Norrköping, Sweden, 2002. 606
Van de Berg, W. J., van den Broeke, M. R., Reijmer, C. H., and van Meijgaard, E.: Characteristics of the Antarctic Surface Mass Balance (1958–2002) Using a Regional Atmospheric

Climate Model, Ann. Glaciol., 41, 97–104, 2005. 606
Van de Berg, W. J., van den Broeke, M. R., and van Meijgaard, E.: Spatial structures in the heat budget of the Antarctic atmospheric boundary layer, The Cryosphere, 2, 1–12, 2008, http://www.the-cryosphere-discuss.net/2/1/2008/. 615, 618
Van den Broeke, M., Smeets, P., Ettema, J., and Kuipers Munnike, P.: Surface radiation balance in the ablation zone of the west Greenland ice sheet, J. Geophys. Res., 113, D13105, doi: 10.1029/2007JD009283, 2008a. 605, 619
Van den Broeke, M., Smeets, P., Ettema, J., van der Veen, C., van de Wal, R., and Oerlemans, J.: Partitioning of melt energy and meltwater fluxes in the ablation zone of the west Greenland ice sheet, The Cryosphere, 2, 179–189, 2008, http://www.the-cryosphere-discuss.net/2/179/2008/.b. 605, 617, 622
Van den Broeke, M. R. and van Lipzig, N. P. M.: Factors controlling the near-surface wind field in Antarctica, Mon. Weather Rev., 131, 733–743, 2003. 608
Van den Broeke, M. R., Duynkerke, P. G., and Oerlemans, J.: The observed katabatic flow at the edge of the Greenland ice sheet during GIMEX-91, Global Planet. Change, 9, 3–15, 1994. 604, 612
Van den Broeke, M. R., van Lipzig, N. P. M., and Van Meijgaard, E.: Momentum budget of the East Antarctic atmospheric boundery layer: results of a regional climate model, J. Atmos. Sci., 59, 3117–3129, 2002. 612
Van den Broeke, M. R., Smeets, P., and Ettema, J.: Surface layer climate and turbulent exchange in the ablation zone of the west Greenland ice sheet, Int. J. Climatol., 2309–2323, doi:10.1002/joc.1815, 2008c. 605, 611, 620, 621
Van Meijgaard, E., van Ulft, L. H., van de Berg, W. J., Bosveld, F. C., van den Hurk, B. J. J. M., Lenderink, G., and Siebesma, A. P.: The KNMI regional atmospheric climate model RACMO version 2.1, Tech. Rep. 302, KNMI, P.O. box 201, 3730 AE, De Bilt, The Netherlands, 2008. 606
White, P. W. (ed.): IFS documentation CY23r4: Part IV physical processes, online available at: http://www.ecmwf.int/research/ifsdocs/, 2004. 606

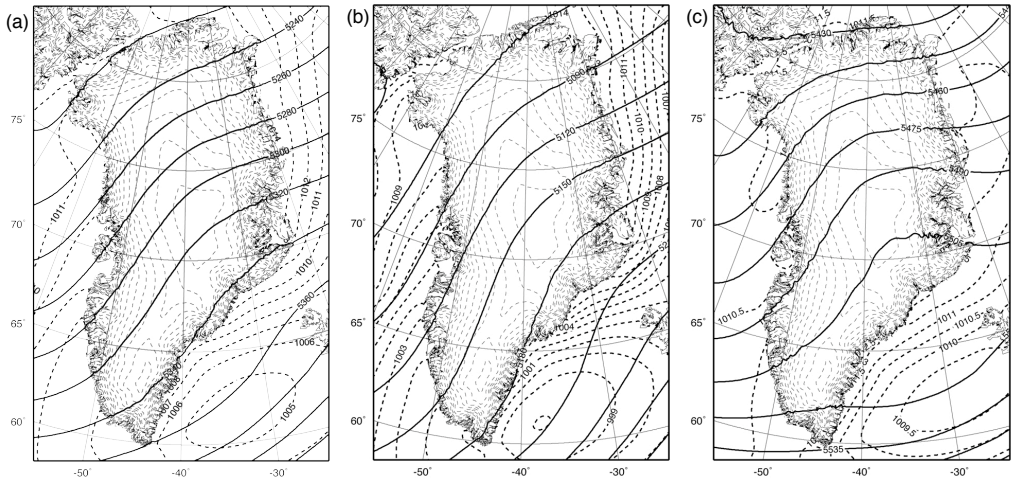

Fig. 1. Mean 500 hPa height Z_{500} [m m.s.l.; solid contours], sea level pressure p_s [hPa; dashed contours over ocean only], topography of the GrIS [m; dashed contours every 250 m over land only] averaged over the **(a)** year, **(b)** winter (DJF), and **(c)** summer (JJA). Note the differences in contour increments.

TCD
4, 603–639, 2010

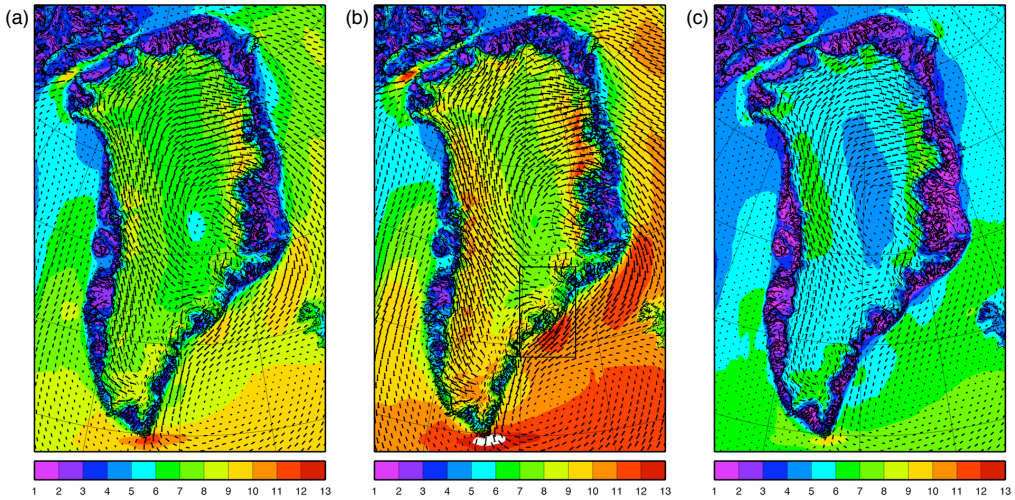

Fig. 2. Averaged 10 m wind speed (contours, [m s^{-1}]) and wind vectors over **(a)** year, **(b)** DJF, and **(c)** JJA. Vectors are plotted every 4 grid points for clarity. Box in (b) indicates region enlarged in Fig. 3b.

TCD
4, 603–639, 2010

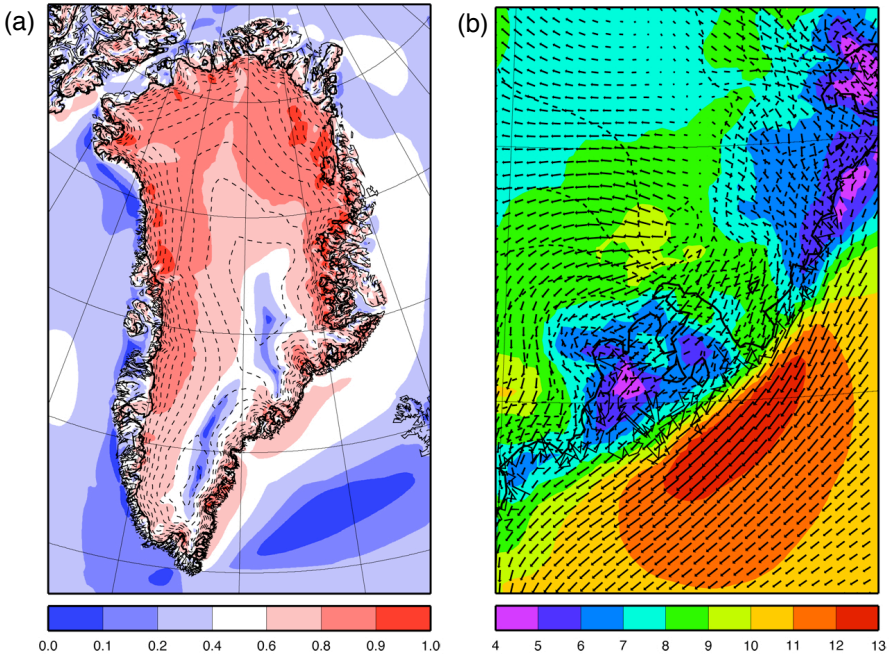

Fig. 3. (a) Directional constancy based on annual wind speed and direction [–], and **(b)** DJF mean of 10 m wind field (vectors [m s^{-1}]) and its magnitude (colouring [m s^{-1}]) plotted at full model resolution for box indicated in Fig. 2b.

TCD
4, 603–639, 2010

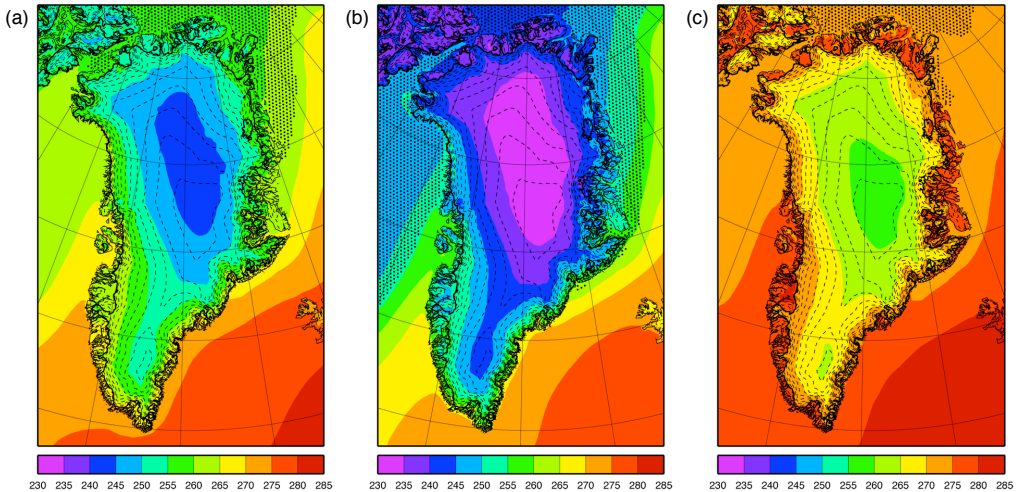

Fig. 4. Averaged 2 m temperature (colour contours, [K]) and sea ice extent (shaded) over **(a)** years, and the seasons **(b)** DJF, **(c)** and JJA.

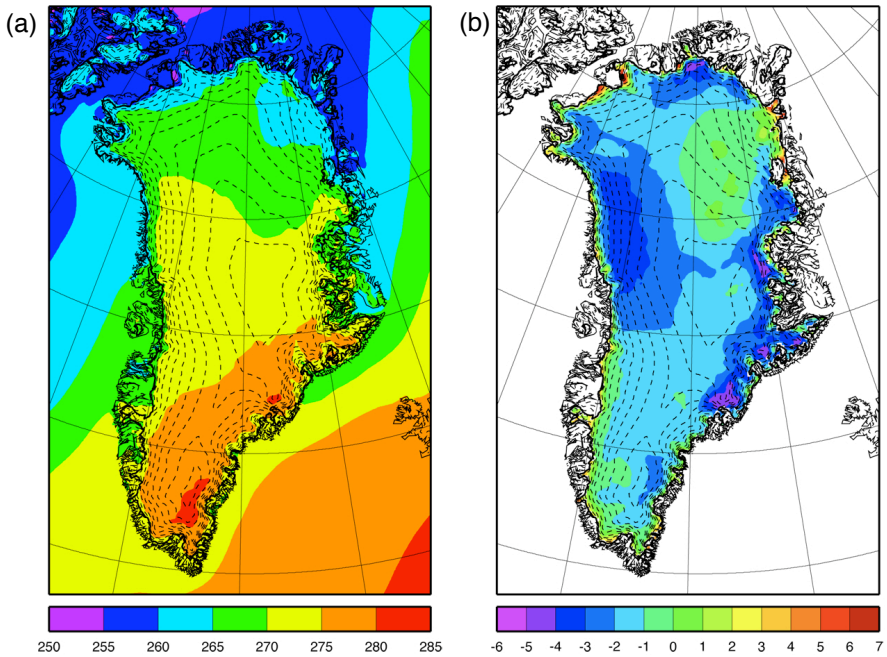

Fig. 5. **(a)** Mean annual 2 m potential temperature [K], and **(b)** difference between $T_{2\ \mathrm{m,Reeh}}$ computed with Eq. (3) and mean annual air 2 m temperature of RACMO2/GR [°C].

TCD
4, 603–639, 2010

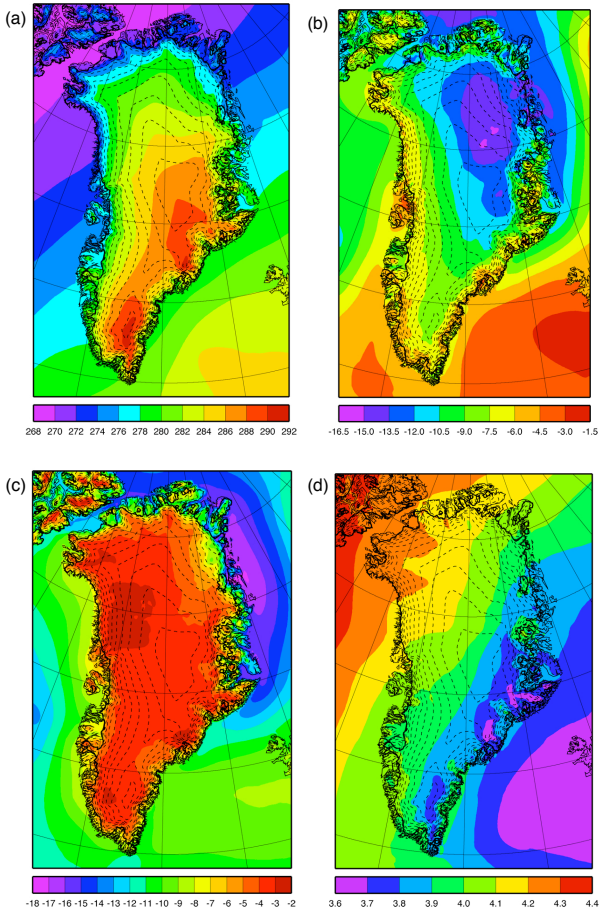

Fig. 6. **(a)** Background surface potential temperature [K], **(b)** annual surface potential temperature perturbation [K], **(c)** annual vertically integrated potential temperature perturbation [10^3 K m], and **(d)** lapse rate of the background potential temperature [K km^{-1}].

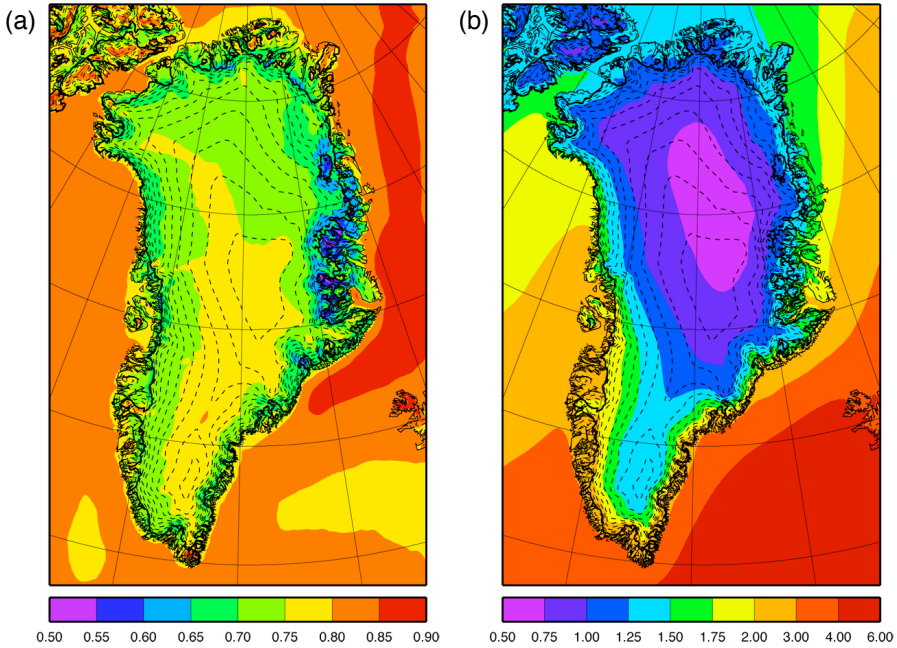

Fig. 7. (a) Annual 2 m relative humidity [–], and **(b)** annual 2 m specific humidity [g kg^{-1}].

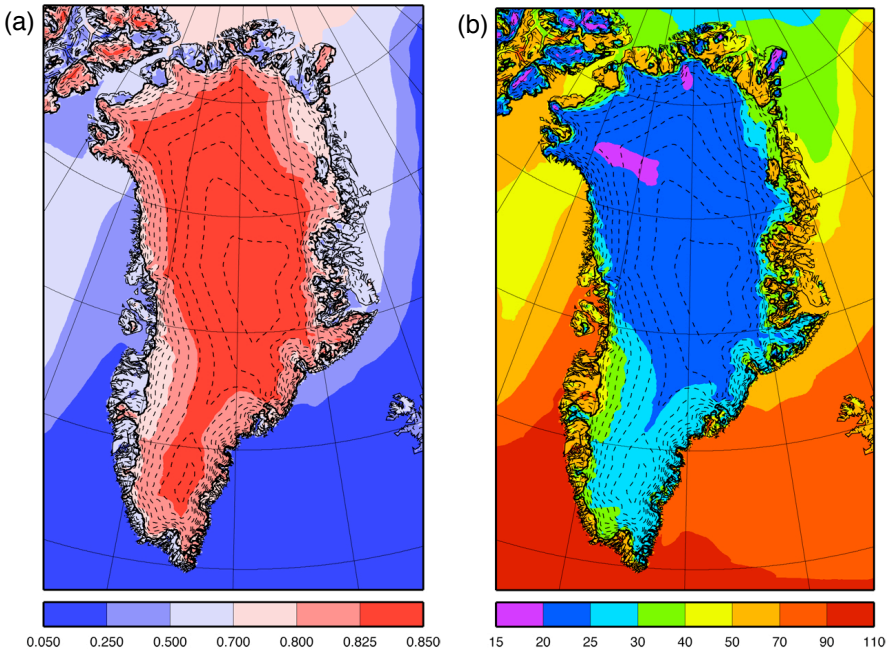

Fig. 8. (a) Mean annual surface albedo [–], and **(b)** net solar radiation [W m^{-2}].

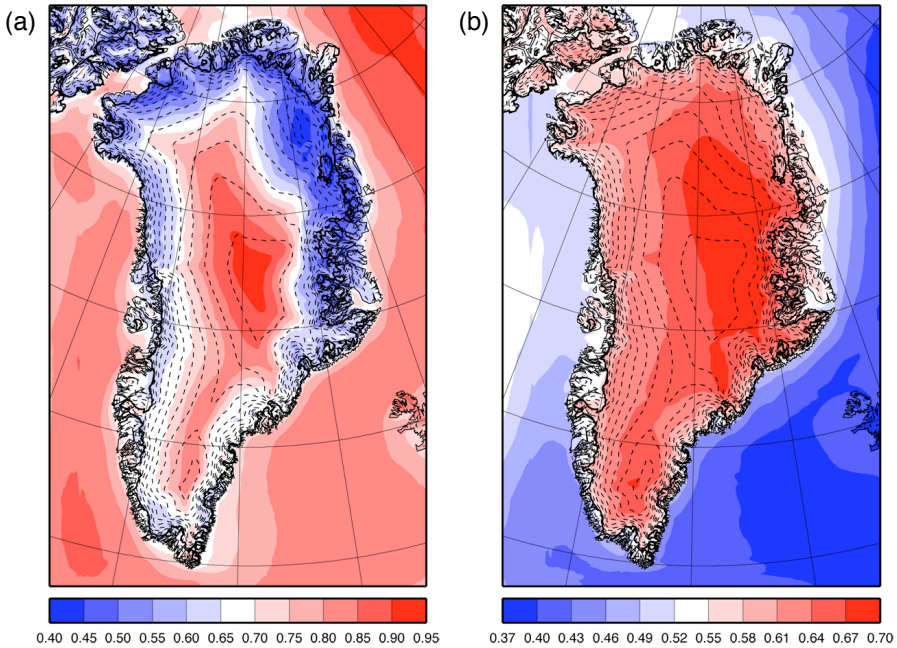

Fig. 9. (a) Annual total cloud cover [−], and **(b)** atmospheric SW transmissivity ($SW_{\downarrow}/SW_{\downarrow,TOA}$) [−].

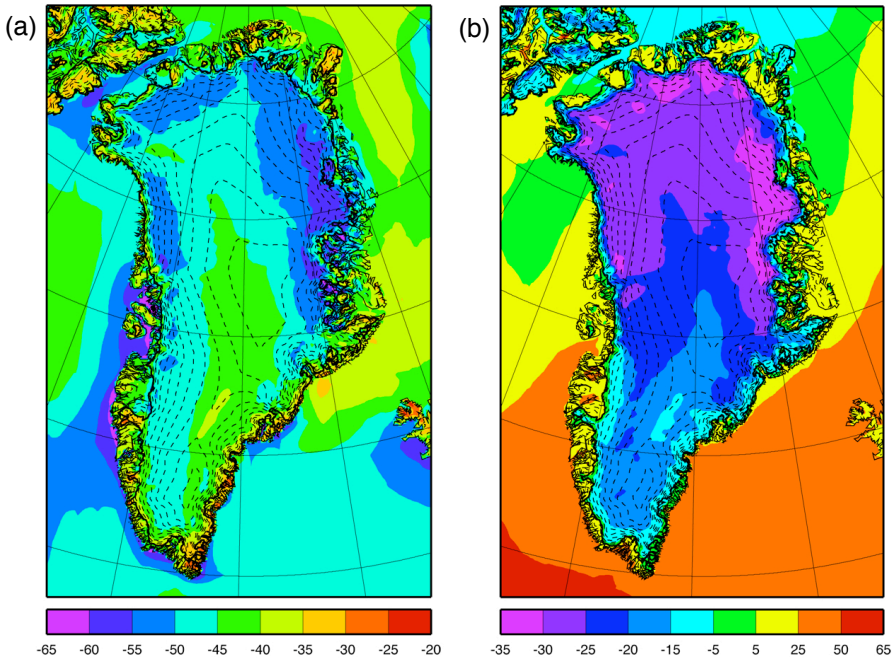

Fig. 10. (a) Mean annual net surface longwave radiation [W m^{-2}], and **(b)** net surface radiation [W m^{-2}].

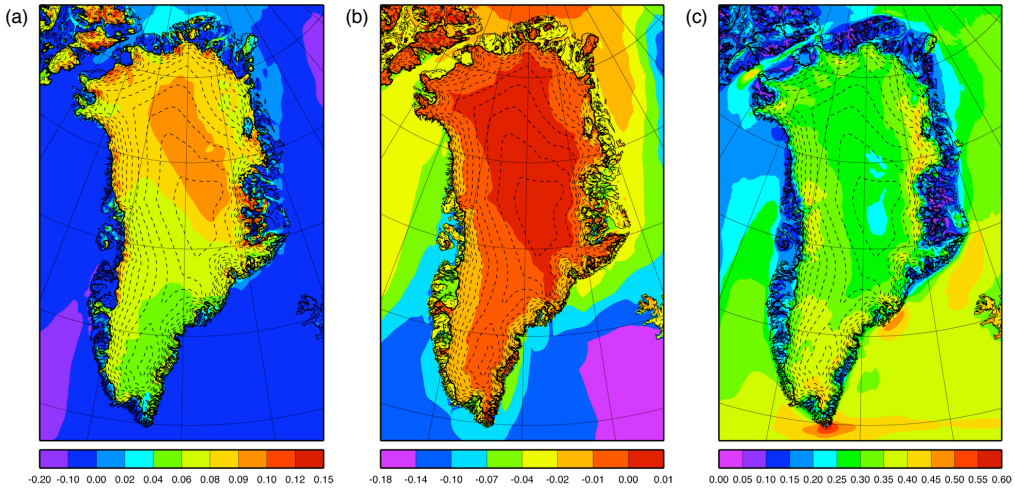

Fig. 11. **(a)** Annual mean turbulent temperature scale θ_* [K], **(b)** turbulent humidity scale q_* [g kg^{-1}], and **(c)** friction velocity u_* [m s^{-1}] over the period 1958–2008.

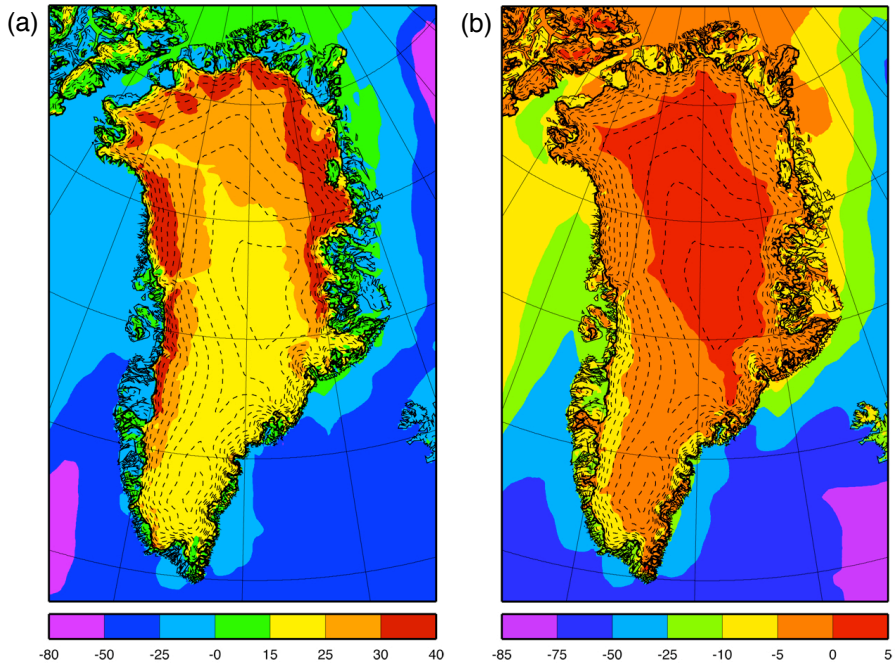

Fig. 12. (a) Annual mean surface sensible heat flux SHF [W m^{-2}], and **(b)** surface latent heat flux LHF [W m^{-2}] over period 1958–2008.

TCD
4, 603–639, 2010

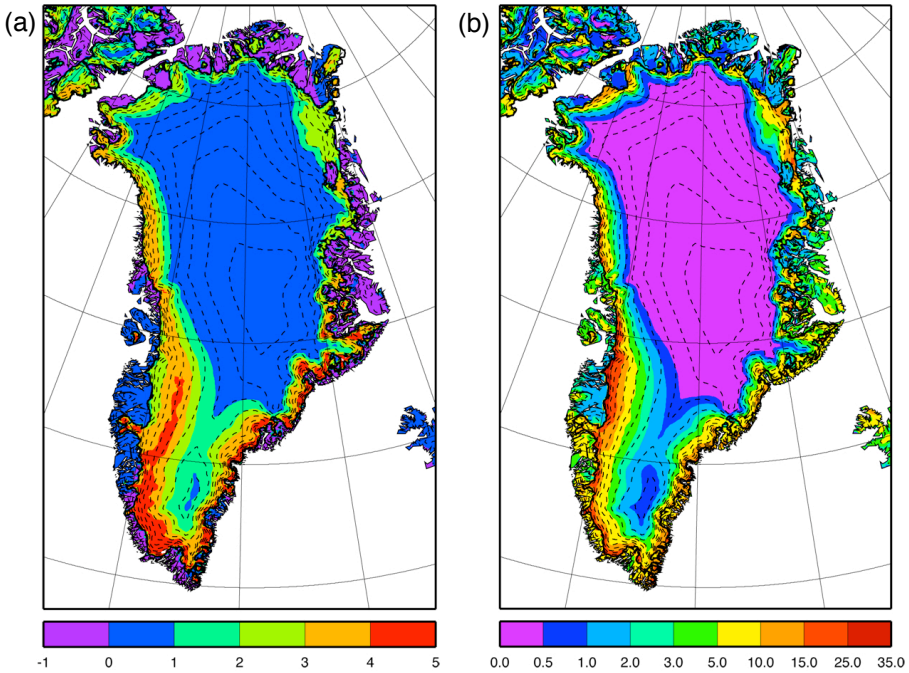

Fig. 13. (a) Mean annual subsurface heat flux G_s [W m^{-2}], and **(b)** melt energy M [W m^{-2}].